Numerical Analysis of Surface-Piercing Propellers

Yin Lu Young[1] and **Spyros A. Kinnas**[2]

ABSTRACT

A 3-D low-order boundary element method, PROPCAV, has been extended to predict unsteady hydrodynamic forces and ventilation patterns on a surface-piercing propeller. The negative image method is used to account for the effect of the free surface. The ventilated cavity patterns at every time step is determined iteratively by satisfying both the kinematic and the dynamic boundary conditions. The detachment locations of the ventilated cavities are determined iteratively by applying a condition similar to the Villat-Brillouin smooth detachment criterion. Finally, the coupling of boundary element method with a finite element method to include hydroelastic effects is presented.

INTRODUCTION

Surface-piercing propellers (also known as partially-submerged propellers) are often recognized as the most fuel-efficient propulsive device for high-speed vessels. Their high efficiency is primarily attributed to the reduction of appendage drag and larger propeller diameter compared to conventional propellers. A comparison of the maximum installed efficiency for different propulsors (taken from (Allison 1978)) is shown in Fig. 1. According to (Hadler & Hecker 1968), the first U.S. patent for a surface-piercing propeller was issued in 1869 to C. Sharp of Philadelphia. It was designed for shallow-draft boat propulsion. As time progressed, surface-piercing propellers were also used for hydroplane boats and high-speed surface effect ships. Due to the superior propulsive characteristics of surface-piercing propellers, they are extensively used today in offshore racing, where speeds often exceed 100 knots (Olofsson 1996). Recently, the commercial marine industry has shown an increased interest for large surface-piercing propellers. They are to be used in the next generation ferries with service speeds in the range of 70 to 80 knots at shaft powers of about 20 MW (Olofsson 2001). Hence, there is a high demand from the marine industry to develop a reliable method that can predict the performance of surface-piercing propellers.

[1]Assistant Professor, Department of Civil and Engineering, PRINCETON UNIVERSITY, Princeton, NJ, 08544. Phone : 609-258-5426 Fax: 609-258-0998 E-mail: yyoung@princeton.edu

[2]Associate Professor, Ocean Engineering Group, Department of Civil Engineering, C1786, THE UNIVERSITY OF TEXAS AT AUSTIN, 1 University Station, Austin, TX 78712. Phone : 512-475-7969 Fax : 512-471-5870 E-mail: kinnas@mail.utexas.edu

Previous Experimental Investigations

In the past, the design of surface-piercing propellers often involved trial and error procedures using the measured performance of test models in free-surface tunnels or towing tanks. One of the first known experimental studies of partially submerged propellers was presented in (Reynolds 1874), where the effect of immersion on skewed propellers was studied. Since then, many more experimental investigations have been published. Notable investigations include studies by (Shiba 1953, Hadler & Hecker 1968, Shields 1968, Hecker & Crown 1970, Brandt 1973, Kruppa 1972, Hecker 1973, Alder & Moore 1977, Rains 1981, Rose & Kruppa 1991, Kruppa 1992, Rose et al 1993, Wang 1995, Ferrando & Scamardella 1996, Nozawa & Takayama 2002a). The focus of all these studies was to determine the *time-averaged* thrust, torque, bending moment, and transverse forces. More recently, (Dobay

1970, Olofsson 1996, Miller & Szantyr 1998, Dyson 2000, Dyson et al 2000, Nozawa & Takayama 2002b) also conducted experiments to determine the dynamic performance of partially submerged propellers. The common objective was to study the *time-dependent* hydrodynamic load, and stresses induced on the propeller blades, shaft, and hull structure.

Based on findings from the above-mentioned experimental studies, it can be generally concluded that there exist three major operating regimes for surface-piercing propellers: partially ventilated, transition, and fully ventilated.

- *Partially-Ventilated Regime:* The air cavities start near the blunt trailing edge and vent toward the free surface. When the advance coefficient is reduced, a partial cavity filled primarily with liquid vapor may also develop. In this flow regime, the extent and volume of the air cavity, as well as the time-averaged thrust and torque coefficients, tend to increase with decreasing advance coefficient.

- *Transition Regime:* When the advance coefficient is further reduced from the partially-ventilated regime, the propeller enters the transition regime. This flow regime is highly unstable, and is accompanied by violent oscillatory forces. The air cavities will start to spread toward the blade leading edge and fluctuate in shape and size. In addition, a sudden drop in thrust and torque coefficients will occur due to spread of air cavities toward blade leading edge.

- *Fully-Ventilated Regime:* When the advance coefficient is further reduced, the propeller enters the fully-ventilated regime. This flow regime is characterized by continuous ventilated cavities that start near the leading edge on the suction side of each blade and vent to the atmosphere. This flow regime is relatively stable and the blade trailing edge remains ventilated at all times. The thrust and torque coefficients tend to decrease with the advance coefficient due to the dominance of cascade effects.

An illustrative drawing of the propeller thrust/torque characteristics in the three major flow regimes is shown in Fig. 2.

Due to the complex phenomena associated with surface-piercing propellers, systematic model tests are extremely expensive, difficult, and time consuming to perform. The test must be carried out in a variable pressure free-surface tunnel that permits high-speed operations to explore the various flow regimes. The free surface must be clearly defined (Kruppa 1992, Rose et al 1993, Olofsson 1996, Dyson 2000). A multi-component dynamometer is needed to measure primary and secondary forces(Hecker & Crown 1970, Dobay 1970, Rose et al 1993, Miller & Szantyr 1998). Special equipments are also needed to simultaneously provide realistic conditions for cavitation inception while maintaining constant water density (Olofsson 1996). Furthermore, special considerations are needed to address scale issues so that the performance of the model scale (including flow and blade vibration characteristics) resembles that of the prototype (Hadler & Hecker 1968, Dobay 1970, Olofsson 1996, Dyson 2000, Nozawa & Takayama 2002b). Thus, the development of reliable, versatile, and robust computational tools to predict propeller performance is crucial to the design and application of partially submerged propellers.

Previous Theoretical Investigations

The development of numerical methods for the analysis and design of surface-piercing propellers has been slow compared to conventional propellers. The main difficulty arises from (1) unknown physics at the blades' entry to, and exit from, the free surface; (2) the development of very thick and very long ventilated cavities that are interrupted by the free surface; and (3) fatigue and vibration effects due to cyclic loading and unloading of the blades associated with the blades' entry to, and exit from, the free surface.

The first known method for the analysis of surface-piercing propellers was developed by (Yegorov & Sadovnikov 1961). He applied a blade element method based on two-dimensional hydrofoil theory, but ignored the effect of adjacent blades, cavities, and wake vortex sheets (Olofsson 1996). Later, (Oberembt 1968) applied a lifting line approach that included the effect of immersion, but the propeller was assumed to be lightly loaded such that no natural ventilation of the propeller and its vortex wake occur. Furuya developed a lifting-line approach that included the effect of propeller ventilation in (Furuya 1984, Furuya 1985). He applied the image method to account for free surface effects. He also assumed the face portion of the blades to be fully wetted and the back portion of the blades to be fully ventilated starting from the blade leading edge. The blades were reduced to a series of lifting lines, and method was combined with a 2-D water entry-and-exit theory developed by (Wang 1977, Wang 1979) to determine thrust and torque coefficients. Furuya compared the predicted mean thrust and torque coefficients with experimental measurements obtained by (Hadler & Hecker 1968). In general, the predicted thrust coefficients were within acceptable range compared to measured values. However, there were significant discrepancies with torque coefficients. Furuya (Furuya 1984, Furuya 1985) attributed the discrepan-

cies to the effects of nonlinearity during the blade entry phase, absence of the blade and cavity thickness representation in the induced velocity calculation, uncertainties in interpreting the experimental data, and limitations of the lifting-line theory.

In 1991, (Vorus 1991) extended the conventional propeller theory given in (Lewis 1989) to determine steady forces and moments on a surface-piercing propeller. He assumed that the steady sectional lift coefficient (ΔC_L) is linearly related to the increment blade section angle of attack ($\Delta\alpha$) as in the case of a fully-ventilated flat plate: $\Delta C_L = \frac{\Pi}{4}\Delta\alpha$. The effects of rake, skew, and inclination in the geometry were considered. The method was shown to be an easy to use design tool for trade-off studies and optimization of blade geometry (Vorus 1991).

An unsteady lifting surface method was employed by (Wang et al 1990a) for the analysis of 3-D fully ventilated thin foils entering into initially calm water. The method was later extended by (Wang et al 1990b, Wang et al 1992) to predict the performance of fully ventilated partially submerged propellers with its shaft above the water surface. Similar to (Furuya 1984, Furuya 1985), the method assumed the flow to separate from both the leading edge and trailing edge of the blade, forming on the suction side a cavity that vents to the atmosphere. Discrete line vortices and sources were placed on the face portion of the blade to simulate the effect of blade loading and cavity thickness, respectively. Line sources were also placed on the cavity surface behind the trailing edge of the blade to represent the cavity thickness in the wake. A helical surface with constant radius and pitch were used to construct the trailing vortex sheets. The negative image method was used to account for free surface effects. The sources representing the blade thickness were neglected in the computation. Comparisons were presented with both experimental measurements by (Hadler & Hecker 1968) and numerical predictions by (Furuya 1984, Furuya 1985). The predictions were within reasonable agreement with experimental values for a propeller with limited data range. However, substantial discrepancies were observed with experimental values and numerical predictions by (Furuya 1984, Furuya 1985) for another propeller.

A 3-D vortex-lattice lifting surface method developed by (Kudo & Ukon 1994, Kudo & Kinnas 1995) for the analysis of supercavitating propellers was extended to treat surface-piercing propellers. However, the method performed all the calculations assuming the propeller to be fully submerged, then multiplied the resulting forces with the propeller submergence ratio. As a result, only an estimate of the mean forces was obtained while the complicated phenomena of blades' entry to, and exit from, the water surface were completely ignored.

A 2-D time-marching boundary element method (BEM) was developed by (Savineau & Kinnas 1995) for the analysis of the flow field around a fully ventilated partially submerged hydrofoil. The negative image method was used to account for free surface effects. However, this method only considered the hydrofoil's entry to, but not exit from, the water surface.

Present Method for Hydrodynamic Analysis

In the present method, a low-order (piecewise constant dipole and source distributions) potential-based boundary element method is used to predict the hydrodynamic performance of surface-piercing propellers. The low-order potential based BEM was first applied for the analysis of marine propellers in steady flow by (Lee 1987, Kerwin et al 1987) and unsteady flow by (Hsin 1990, Kinnas & Hsin 1992). The method was then extended for the analysis of flow around 2-D partially and supercavitating hydrofoils (Kinnas & Fine 1991) and 3-D partially cavitating hydrofoils (Fine & Kinnas 1993a). In (Kinnas & Fine 1992), the method was named PROPCAV (PROPeller CAVitation) for its added ability to analyze 3-D unsteady flow around cavitating propellers. Later, (Mueller & Kinnas 1999) modified the method to search for midchord cavitation on either the back or the face of propeller blades. Recently, the method was further extended to predict alternating or simultaneous face and back cavitation for classical (Young & Kinnas 2001) and supercavitating (Young & Kinnas 2003b) propeller blades operating in fully submerged conditions.

OBJECTIVE

The objective of this research is to modify PROPCAV to predict the performance of surface-piercing propellers. Preliminary results were presented in (Young & Kinnas 2000), which made the following simplifications: (1) the suction side geometry aft of the midchord was modified to render zero trailing edge thickness, (2) the blades were assumed to be fully ventilated starting from the blade leading edge, and (3) the blades were assumed to be infinitely rigid (i.e. the effects of blade vibrations were ignored). In this work, the actual blade geometry with the non-zero trailing edge thickness is modeled, the detachment locations of the ventilated cavities are searched for iteratively, and a coupling algorithm to include hydroelastic effects is presented. The goal is to develop a robust and reliable tool to predict the hydro- and elasto-dynamic performance of surface-piercing propellers.

HYDRODYNAMIC FORMULATION

The formulation for surface-piercing propellers is very similar to that for submerged propellers, which is given in (Kinnas & Fine 1992, Young & Kinnas 2001). It is summarized here for the sake of completeness.

Consider a surface-piercing propeller subject to a general inflow wake $\vec{q}_w(X,Y,Z)$ as shown in Fig. 3. The inflow wake is expressed in terms of the absolute (ship fixed) system of coordinates (X,Y,Z), and is assumed to be the *effective wake*, i.e. it includes the interaction between the vorticity in the inflow and the propeller (Kinnas et al 2000, Choi 2000). The inflow velocity, $\vec{q}_{in}$, with respect to the propeller fixed coordinates (x,y,z), can be expressed as the sum of the inflow wake velocity, $\vec{q}_w$, and the propeller's angular velocity $\vec{\omega}$, at a given location $\vec{x}$:

$$\vec{q}_{in}(x,y,z,t) = \vec{q}_w(x,r,\theta_B - \omega t) + \vec{\omega} \times \vec{x} \qquad (1)$$

where $r = \sqrt{y^2+z^2}$, $\theta_B = \arctan(z/y)$, and $\vec{x} = (x,y,z)$. The resulting flow is assumed to be incompressible and inviscid. Hence, the total velocity, $\vec{q}$, can be expressed in terms of $\vec{q}_{in}$ and the perturbation potential ϕ:

$$\vec{q}(x,y,z,t) = \vec{q}_{in}(x,y,z,t) + \nabla\phi(x,y,z,t) \qquad (2)$$

where ϕ satisfies the Laplace's equation in the fluid domain (i.e. $\nabla^2\phi = 0$). Note that the propeller fixed coordinates system is used in analyzing the flow.

The Boundary Integral Equation

The perturbation potential, ϕ_p, at every point p on the combined wetted blade surface $S_{WB}(t)$, ventilated cavity surface $S_C(t) = S_{C1}(t) \cup S_{C2}(t) \cup S_{C3}(t)$, and free surface $S_F(t)$, must satisfy Green's third identity:

$$2\pi\phi_p(t) = \int\int_{S(t)} \left[\phi_q(t) \frac{\partial G(p;q)}{\partial n_q(t)} - G(p;q) \frac{\partial \phi_q(t)}{\partial n_q(t)} \right] dS \qquad (3)$$

where $S(t) \equiv S_{WB}(t) \cup S_C(t) \cup S_F(t)$ is the combined surfaced as defined in the blade section example shown on Fig. 4. The subscript q corresponds to the variable point in the integration. $G(p;q) = 1/R(p;q)$ is the Green's function with $R(p;q)$ being the distance between points p and q. $\vec{n}_q$ is the unit vector normal to the integration surface, with the positive direction pointing into the fluid domain.

Equation 3 should be applied on the "exact" ventilated cavity surface S_C, as shown in Fig. 4. However, the ventilated cavity surface is not known and has to be determined as part of the solution. In this work, the ventilated cavity surfaces are approximated with the blade surface underneath the cavity, $S_{C2}(t) \rightarrow S_{CB}(t)$, and the portion of the wake surface which is overlapped by the cavity, $S_{C1}(t) \cup S_{C3}(t) \rightarrow S_{CW}(t)$. The definition of $S_{CB}(t)$ and $S_{CW}(t)$ are also shown in Fig. 4. The justification for making this approximation, as well as a measure of its effect on the cavity solution can be found in (Kinnas & Fine 1993, Fine 1992).

Boundary Conditions

• *Kinematic and Dynamic B.C. on the Free Surface*

On the exact free surface, the dynamic boundary condition requires the pressure everywhere on the free surface to be constant and equal to the atmospheric pressure, and the kinematic boundary condition requires the normal velocities of the fluid and of the free surface to be equal. In the present method, the linearized form of the combined free surface kinematic and dynamic boundary conditions is applied:

$$\begin{aligned} \frac{\partial^2\phi}{\partial t^2}(x,y,z,t) + g\frac{\partial\phi}{\partial y_s}(x,y,z,t) &= 0 \qquad (4) \\ \text{at} \qquad Y &= -R+h \end{aligned}$$

where h and R are the blade tip immersion and blade radius, respectively, as defined in Fig. 5. Y is the vertical ship-fixed coordinate, also defined in Fig. 3.

Assuming that the infinite Froude number condition (i.e. $F_r = V/\sqrt{gD} \rightarrow \infty$) applies, Eqn. 4 reduces to:

$$\phi(x,y,z,t) = 0 \qquad \text{at} \qquad Y = -R+h \qquad (5)$$

The above equation implies that the negative image method can be used to account for the effect of the free surface. Consequently, only vertical motions are allowed on the free surface. This is accomplished by distributing sources and dipoles of equal strengths but with negative signs on the location of the mirror image with respect to the free surface. A schematic example of the negative image method on a blade section is shown in Fig. 6.

• *Kinematic B.C. on Wetted Blade Surfaces*

The kinematic boundary condition requires the flow to be tangent to the wetted blade surfaces, which forms a Neumann-type boundary condition for $\frac{\partial\phi}{\partial n}$:

$$\frac{\partial\phi}{\partial n} = -\vec{q}_{in} \cdot \vec{n} \qquad (6)$$

• *Dynamic B.C. on Ventilated Cavity Surfaces*

The dynamic boundary condition requires that the pressure everywhere on the ventilated cavity surface to be constant and equal to the atmospheric pressure, P_{atm}. Defining $\sigma_a \equiv (P_o - P_{atm})/(\frac{\rho}{2}n^2D^2)$ as the ventilation number, the total ventilated cavity velocity, $\vec{q}_c$, can be expressed as follows:

$$|\vec{q}_c|^2 = n^2D^2\sigma_a + |\vec{q}_w|^2 + \omega^2r^2 - 2gY - 2\frac{\partial\phi}{\partial t} \qquad (7)$$

where ρ is the fluid density and r is the distance from the axis of rotation. P_o is the pressure far upstream on the shaft axis; g is the acceleration of gravity and Y is the ship fixed coordinate. $n = \omega/2\pi$ and D are the propeller rotational frequency and diameter, respectively.

The total ventilated cavity velocity can also be expressed in terms of the local derivatives along the s (chordwise), v (spanwise), and n (normal) grid directions:

$$\vec{q}_c = \frac{V_s\left[\vec{s} - (\vec{s}\cdot\vec{v})\vec{v}\right] + V_v\left[\vec{v} - (\vec{s}\cdot\vec{v})\vec{s}\right]}{||\vec{s}\times\vec{v}||^2} + (V_n)\,\vec{n} \quad (8)$$

where $\vec{s}$, $\vec{v}$, and $\vec{n}$ denote the unit vectors along the non-orthogonal curvilinear coordinates s, v, and n, respectively. The total velocities on the local coordinates (V_s, V_v, V_n) are defined as follows:

$$V_s \equiv \frac{\partial\phi}{\partial s} + \vec{q}_{in}\cdot\vec{s};\;\; V_v \equiv \frac{\partial\phi}{\partial v} + \vec{q}_{in}\cdot\vec{v};\;\; V_n \equiv \frac{\partial\phi}{\partial n} + \vec{q}_{in}\cdot\vec{n} \quad (9)$$

Note that if s, v, and n were located on the "exact" ventilated surface, then the total normal velocity, V_n, would be zero. However, this is not the case since the cavity surface is approximated with the blade surface beneath the cavity and the wake surface overlapped by the cavity. Although V_n may not be exactly zero on the approximated cavity surface, it is small enough to be neglected in the dynamic boundary condition (Fine 1992).

Equations 7 and 8 can be integrated to form a quadratic equation in terms of the unknown chordwise perturbation velocity $\frac{\partial\phi}{\partial s}$. By selecting the root which corresponds to the cavity velocity vectors that point downstream, the following expression can be derived:

$$\frac{\partial\phi}{\partial s} = -\vec{q}_{in}\cdot\vec{s} + V_v\cos\psi + \sin\psi\sqrt{|\vec{q}_c|^2 - V_v^2} \quad (10)$$

where ψ is the angle between s and v directions. Equation 10 can then integrated to form a Dirichlet type boundary condition for ϕ. It should be noted that the terms $\frac{\partial\phi}{\partial t}$ and $\frac{\partial\phi}{\partial v}$ inside $|\vec{q}_c|$ and V_v in Eqn. 10 are also unknown and are determined in an iterative manner.

On the ventilated wake surface, the coordinate s is assumed to follow the streamlines. It was found that the crossflow term $(\frac{\partial}{\partial v})$ in the cavitating wake region had a very small effect on the solution (Fine 1992, Fine & Kinnas 1993b). Thus, the total cross flow velocity is assumed to be small, which renders the following expression on the ventilated wake surface:

$$\frac{\partial\phi}{\partial s} = -\vec{q}_{in}\cdot\vec{s} + |\vec{q}_c| \quad (11)$$

• *Kinematic B.C. on the Ventilated Cavity Surfaces*

The kinematic boundary condition requires that the total velocity normal to the ventilated cavity surface to be zero:

$$\begin{aligned} \frac{D}{Dt}(n - h(s,v,t)) &= 0 \quad (12)\\ \left[\frac{\partial}{\partial t} + \vec{q}_c(x,y,z,t)\cdot\nabla\right](n - h(s,v,t)) &= 0 \end{aligned}$$

where n and h are the curvilinear coordinate and ventilated cavity thickness normal to the blade surface, respectively.

Substituting Eqn. 8 into Eqn. 12 yields the following partial differential equation for h on the blade surface (Kinnas & Fine 1992):

$$\frac{\partial h}{\partial s}\left[V_s - \cos\psi V_v\right] + \frac{\partial h}{\partial v}\left[V_v - \cos\psi V_s\right] = \sin^2\psi\left(V_n - \frac{\partial h}{\partial t}\right) \quad (13)$$

For surface-piercing propellers, the cross-flow velocities are also assumed to be small on the blade surface (i.e. $V_v \approx V_s\cos\psi$ on $S_{CB}(t)$), which reduces the $\frac{\partial h}{\partial v}$ term in Eqn. 13 to zero. The justification of this assumption can be found in (Fine 1992), where it is shown that the cross-flow term (evaluated iteratively) on the blade has a very small effect on the predicted supercavity on either a 3-D hydrofoil or a propeller blade.

NUMERICAL IMPLEMENTATION OF BEM

For surface-piercing propellers, Green's formula (Eqn. 3) is only solved for the total number of submerged panels on the *key* blade and the ventilated portion of the *key* wake. The influence of each of the other blades is accounted for in a progressive manner by using the solution from an earlier time step when the key blade was in the position of that blade. The values of ϕ and $\frac{\partial\phi}{\partial n}$ are set equal to zero on the blade and wake panels that are above the free surface. Note that the current algorithm does not re-panel the blades and wakes at every time step in order to maintain computation efficiency. As a result, there are some panels that are partially cut by the free surface. In the present algorithm, the strengths of the singularities are also set equal to zero for the partially submerged panels. Nevertheless, a method similar to the split-panel technique (Kinnas & Fine 1993) can be applied to account for the effects of these panels.

The time marching scheme is similar to that described in (Fine 1992). A constant time increment, Δt, is used. At each time step, the propeller blades rotate by a blade angle increment $\Delta\theta = \omega\Delta t$. Notice that in

Eqns. 10 and 11, the $\frac{\partial \phi}{\partial t}$ term inside $|\vec{q}_c|^2$ is assumed to be known. In the current algorithm, it is given by a second order moving least square derivative recovery method (Tabbara et al 1994) using the solution (ϕ) obtained from the previous revolution.

The numerical implementation is described in detail in (Young 2002, Young & Kinnas 2003a, Young & Kinnas 2003c). In brief, for a given cavity planform, Green's formula , Eqn. 3, is solved with respect to unknown ϕ on wetted blade surfaces, and unknown $\frac{\partial \phi}{\partial n}$ on ventilated cavity surfaces. The ventilated cavities are assumed to vent to the atmosphere and their heights are determined by differentiating Eqn. 13 with a second order central finite difference method.

Non-Zero Thickness Blade Trailing Edge

As observed in experiments, the ventilated cavities are assumed to vent to the atmosphere. The pressure behind the blade trailing edge (also called the base pressure) is assumed to be constant and equal to the atmospheric pressure. To avoid "openness" at the blade trailing edge, a small initial closing zone, shown in Fig. 7, is introduced. The precise geometry of the initial closing zone is not important because surface-piercing propellers always operate in superventilated or base-ventilated conditions. Details of the numerical algorithm and systematic parametric studies are presented in (Young 2002, Young & Kinnas 2003b).

Ventilated Cavity Detachment Condition

Depending on the flow conditions and the blade section geometry, the ventilated cavities may detach aft of the blade leading edge. Thus, the ventilated cavity detachment locations on the suction side of the blade are searched for iteratively at each time step until all of the following conditions are satisfied:

- The ventilated cavities have non-negative thickness at their leading edge,
- The pressure on the wetted portion of the blade upstream of the ventilated cavity should be greater than the atmospheric pressure,
- The ventilated cavities must detach at or prior to the blade trailing edge; and
- When the blade departs from the the water, the ventilated cavities must detach at or aft of the intersection between the blade section and the free surface.

It should be noted that the first two criterion are equivalent to the Villat-Brillouin smooth detachment condition (Brillouin 1911, Villat 1914) at zero cavitation number; while the last two criterion are physical constraints for surface-piercing propellers. A schematic diagram showing different ventilated cavity detachment locations for a surface-piercing blade section is depicted in Fig. 8. The pressure on the ventilated cavities are assumed to be constant and equal to the atmospheric pressure. The ventilated cavities can detach anywhere on the suction side of the blade surface, but must detach from the blade trailing edge on the pressure side. It is possible to also search for ventilated cavity detachment locations on the pressure side. However, such occurrence is unlikely due to the high-speed operation of partially submerged propellers.

Wake Alignment

Due to the presence of the free surface, the inflow wake is highly non-axisymmetric. In order to properly align the wake geometry at every time step, an unsteady iterative wake alignment scheme is needed. In (Lee 2002, Lee & Kinnas 2002), the current 3-D potential-based BEM is applied to align the wake geometry by requiring the force-free condition to be satisfied on the wake surface at every time step. However, at the present time, the unsteady wake alignment scheme is limited to fully submerged propellers. Thus, in the present analysis of surface-piercing propellers, the wake is aligned with the inflow velocity when the blade is at the six o'clock position, i.e. at the angular position where the blade's submerged area is maximum. The wake is aligned using an iterative lifting surface method developed by (Greeley & Kerwin 1982), which assumes the blades to be fully submerged and the inflow to be axisymmetric. In addition, the effects of wake roll-up and developed tip vortex cavity are ignored in the present algorithm. Although the present wake alignment scheme for surface-piercing propellers is much simplified from actual conditions, it represents a first step toward predicting the complex behavior of surface-piercing propellers. A more realistic wake alignment scheme, such as that presented in (Lee 2002, Lee & Kinnas 2002), can be added later to refine the performance predictions.

VALIDATION OF BEM CODES

To validate the treatment of surface-piercing propellers, numerical predictions for propeller model 841-B are compared with experimental measurements collected by (Olofsson 1996). A photograph of the surface-piercing propeller and the velocity distribution at the propeller plane is shown in Figs. 9 and 10, respectively. The axial velocity is zero at the free surface because a flat plate was placed in front of the propeller to provide a well defined free surface. Details of the experiments are given in (Olofsson 1996), and are summarized here for the sake of completeness.

Summary of Experiment by Olofsson

In (Olofsson 1996), Olofsson presented a very thorough series of experimental studies to determine the time-averaged and dynamic performance of propeller model 841-B. The four-bladed high-speed partially submerged propeller was designed based on sea trials on a board a 13 m twin screw planing test craft. The diameter of the full-scale propeller is 250 mm. The experiments were conducted at the KaMeWa free surface cavitation tunnel in Sweden. The tunnel was equipped with a large de-aerating chamber downstream of the test section. The de-aerating chamber was used to eliminate the occurrence of air-liquid mixture in the test section when testing to maintain constant water density. The tunnel has also been equipped with a special device for micro air bubble seeding to provide constant cavitation inception as well as realistic propeller thrust and torque without hysteresis in partially cavitating conditions. The blade dynamometer was a 4-bladed, single flexure, 5-component dynamometer developed KaMeWa. It was specially designed to capture the true effect of blade vibration.

In the experiment, only one blade tip immersion ratio ($h/D = 0.33$) was considered, and the influence of Froude and cavitation number at different advance coefficients, $J_A = V/nD$, was systematically investigated. Tests with different shaft yaw and inclination angles were also performed. Three scale models were examined: λ (ratio of full-scale diameter and model scale diameter) = 1, 3, and 9. The model scale was require to have the same cavitation number ($\sigma = (P_o - P_v)/0.5\rho V^2$) and Froude number ($F_r = V/\sqrt{gD}$) as the full scale:

$$\sigma = \frac{P_{atm} - P_v}{0.5\rho g D} \cdot \frac{1}{\lambda} \cdot \frac{1}{F_r^2} \tag{14}$$

where P_v is the vapor pressure, and D is the model scale diameter.

Dynamic Performance: $J_A = 1.2$

At $J_A = 1.2$, the propeller is in the partially ventilated flow regime. The observed ventilation patterns at three different blade angles for $F_r = 6$ and $\lambda = 9$ are shown in Fig. 11. Also shown in Fig. 11 are the predicted ventilation patterns at the same blade angles. At this advance coefficient, both the Froude number and cavitation number affect the dynamic propeller performance. The dependence of the per-blade axial force coefficients, K_{Fx}, on the Froude number and cavitation number is shown in Fig. 12. For $F_r > 4$, the effect of Froude number is negligible. For $F_r \leq 4$, much more scattering of the data can be observed and the blade forces tend to increase with decreasing Froude number during the in-water phase. Similar patterns were also observed in experimental investigations by (Shiba 1953, Shields 1968). Olofsson explained that air is sucked down to a smaller depth at lower Froude numbers, thus lead to higher blade forces due to increase in wetted blade area (Olofsson 1996). The dependence of the per-blade forces on the cavitation number (expressed via scale ratio) is also shown in Fig. 12. At $F_r = 6$, $\lambda = 1, 3, 9$ correspond to $\sigma = 2.3, 0.76, 0.25$, respectively, via Eqn. 14. For $\sigma \geq 0.76$, the effect of cavitation number was negligible, i.e. the cavities were primarily air-filled. However, the blade forces decreased in the exit half of the revolution for $\sigma = 0.25$, which Olofsson (Olofsson 1996) attributed to the development of a vapor-filled cavity near the blade tip region. The heavy solid lines in Fig. 12 represent the predicted axial force coefficient using the current BEM, which assumes the blades to be perfectly rigid and the cavities to be air-filled. Comparisons of the measured and predicted dynamic blade force and moment coefficients for $F_r = 6$ and $\sigma = 2.3$ ($\lambda = 1$) are shown in Fig. 13. The solid lines and the symbols represent the predicted and measured values, respectively. The six components of the individual blade loads, (K_{Fx}, K_{Fy}, K_{Fz}, K_{Mx}, K_{My}, K_{Mz}), are defined according to the coordinate system shown in Fig. 3. The vertical per-blade force coefficient, K_{Fy}, is not shown in Fig. 13 because it was not measured during the experiment. As shown in the figures, the predicted values agreed well with experimental measurements for $J_A = 1.2$.

Dynamic Performance: $J_A = 0.8$

For $J_A = 0.8$, the propeller is in the fully ventilated flow regime. The dependence of the per-blade axial force coefficients on the Froude number and cavitation number is shown in Fig. 14. At $F_r = 6$, $\lambda = 1, 3, 9$ correspond to $\sigma = 2.3, 0.76, 0.25$, respectively, via Eqn. 14. As shown in Fig. 14, the effect of cavitation number is negligible on the dynamic blade performance, which implies that all the cavities are air-filled in the fully ventilated flow regime. This pattern is consistent with other experimental studies by (Shiba 1953, Shields 1968). However, the Froude number affects the dynamic blade performance. The amplitude of the "humps" (amplified fluctuations superimposed on the basic load) increased with increasing Froude number. Similar humps were also observed in unsteady per-blade force measurements of surface-piercing propellers presented in (Miller & Szantyr 1998, Dyson 2000, Dyson et al 2000). Olofsson (Olofsson 1996) stated that for propeller model 841-B, the frequency of these fluctuations modulated between the blade's fundamental frequency in air (1100 Hz) and in water (550 Hz). Thus, it can be concluded that these

humps are associated with resonant blade vibration. Comparisons of the measured and predicted dynamic blade force and moment coefficients for $F_r = 6$ and $\sigma = 2.3$ ($\lambda = 1$) are shown in Fig. 15. As shown in the figure, the predicted values are in reasonable agreement with experimental measurements, but more discrepancies can be observed compared to the results for $J_A = 1.2$ shown in Fig. 13. The discrepancies can be attributed to the inability of the present BEM to model the effects of blade vibration, jet sprays, and rise in overall free surface elevation. In the current BEM formulation, the blades are assumed to be rigid, thus the effects of blade vibrations cannot be captured. In addition, the present method significantly under-predicted the dynamic blade loads at the blade entry phase and exit phase. This discrepancy can be attributed to rise in overall free surface elevations due to cavity displacement effects, and increase in intensity and height of jet sprays. For propeller model 841-B with a blade tip immersion ratio (h/D) of 0.33, the blade leading edge should enter the water at 88 degrees, and the blade trailing edge should exit the water at 272 degrees. However, experimental measurements shown in Fig. 15 suggest that the blade carried load from approximately 68 degrees to 290 degrees. This clearly indicates an increase in overall free surface elevation. In addition, more discrepancies can be observed at the blade entry phase than at the blade exit phase. This is probably due to the fact that strong jets develop near the blade leading edge at the instant of impact, which lead to very high slamming forces at the blade entry phase. In the blade exit phase, sheets of entrained water are carried by the blades to the air, which in turn increase the blade loads due to added wetted blade area. Experimental investigations by (Hadler & Hecker 1968) suggested that the amount of entrained water exiting with the blade is approximately 7-12% of the volume. In the in-water phase, the present method over-predicted the blade forces. One possible explanation is that cascade effects begin to dominate as the thickness of the ventilated cavities increases. In the present method, the singularities are placed on the blade surface beneath the ventilated cavities and the wake surface overlapped by the ventilated cavities. However, when the ventilated cavities become very thick, the use of the approximated ventilated cavity surface may not be appropriate.

Time-Averaged Performance

The predicted and measured time-averaged thrust (K_T), torque (K_Q), and efficiency (η) of propeller model 841-B in the ship-fixed coordinates is shown in Fig. 16. The lines and symbols in Fig. 16 represent the numerical predictions and experimental measurements, respectively. For each advance coefficient, multiple experimental data points are shown to depict the effect of Froude number and cavitation number.

Comparison of the predicted and measured averaged individual blade force and moment coefficients over the advance coefficient squared in the blade-fixed coordinates is shown in Fig. 17. This plot is intended to show how the actual blade forces vary with shaft rate at a given advance coefficient and diameter. For submerged propellers, the force and moment coefficients over advance coefficient squared tend to be linear functions of advance coefficient. As suggested by (Olofsson 1996), the advance coefficient where transition occurred can be observed via the discontinuity of the slope of the curves shown in Fig. 17, which is approximately at $J_A = 0.9$. Figure 17 indicates that K_{Fz} is approximately 20% of K_{Fx}, and K_{Mz} is approximately two times higher than K_{Mx}. The high tangential forces and moments are typical of surface-piercing propellers.

Convergence Study

In order to validate the performance prediction of the BEM, convergence studies with varying numbers of propeller revolutions, panel discretization, and time step size are presented. All the convergence studies shown in this section are for propeller model 841-B with $J_A = 1.2$.

• *Convergence with Number of Revolutions*

The influence of the other blades on the key blade are accounted for in a progressive manner. In addition, iterations are needed to determine the correct ventilated cavity detachment locations. Thus, the solution depends on the number of propeller revolutions. The convergence of individual blade forces with number of revolution for propeller model 841-B is shown in Fig. 18. It should be noted that the unsteady term ($\frac{\partial \phi}{\partial t}$) is not activated until two revolutions are completed for the case of partially submerged propellers to avoid stability problems. As shown in Fig. 18, the results converged very quickly with number of revolutions.

• *Convergence with Time Step Size*

Partially submerged propeller flows are inherently unsteady due to the loading and unloading of the blades associated with the blades' entry to, and exit from, the free surface. Thus, the solution also depends on the time step size, which is expressed in terms of blade angle increment. In Fig. 19, the convergence of the individual blade forces and ventilation patterns for $\Delta\theta = 3^o - 12^o$ are presented. Notice that the results

converged quickly with time step size.

• *Convergence with Grid Size*

In addition to the number of propeller revolutions and blade angle increments, the solution also depends on the panel discretization. Figure 20 depicts the influence of panel discretization on the individual blade forces and ventilation patterns, which also converged quickly with number of panels.

FLUID-STRUCTURE COUPLING

As shown in the previous section, blade vibration is a serious concern for surface-piercing propellers. Blade vibration can significantly affect the hydrodynamic performance of the propeller due to the motion and deformation of the blades. In addition to changes in inertial and gravitational loads, blade vibration also affects the ventilation pattern, as demonstrated in Fig. 21. Furthermore, it has been concluded in the past that the dynamic load on propeller blades is closely related to the fatigue fracture of blades (Dashnaw & Reed 1971, Helle & Hageman 1980). The problem is particularly severe at the thin leading edge of surface-piercing blades, which tend to absorb most of the impact pressure during the blade entry phase. Thus, the modeling of dynamic blade stresses and deformations is crucial for the analysis and design of surface-piercing propellers.

In the past, most structural models applied the modified beam theory to determine blade stresses. The beam theory for blade stress analysis was developed by D.W. Taylor (Taylor 1933) before 1920, which assumed the blade to be a cantilever beam loaded by thrust and torque distributed linearly over the radius (Schoenherr 1963). Later, modifications were made to include the effects of rake, skew, and centrifugal force (Morgan 1954, Schoenherr 1963, Atkinson 1968). However, the beam theory cannot accurately predict the stress distributions for complex blade geometries (e.g. highly skewed propellers, supercavitating propellers, etc) due to its simplified assumptions. More sophisticated theoretical models based on the measured or calculated mode shapes and resonance frequencies of propeller blades in air have been developed by (Tsushima 1972, Brooks 1980). However, these methods were not refined enough for detailed stress analysis (Kuo & Vorus 1985). Recently, finite element methods (FEMs) coupled with hydrodynamic models have also been employed for the analysis of dynamic blade stresses. These include the works of (Genalis 1970) using thin shell elements, (Atkinson 1973) using thick shell elements, and (Kuo & Vorus 1985) using 3-D isoparametric brick elements. However, all of these methods were developed for analysis of submerged, non-cavitating propellers. Most recently, (Dyson 2000, Dyson et al 2000) applied a 3-D FEM using a combination of 2-D semi-loof shell elements and 3-D brick elements for the hydroelastic analysis of surface-piercing propellers. However, it cannot provide accurate description of the dynamic stresses due to the used of assumed hydrodynamic load models (Dyson 2000, Dyson et al 2000). Thus, a consistent coupled hydrodynamic/structural model is needed to determine the dynamic response of surface-piercing propellers.

In this work, a 3-D FEM is coupled with the present BEM to determine the dynamic blade stresses and deformations of surface-piercing propellers. The field decompositions follows the works of (Vorus 1981, Kuo & Vorus 1985), but additional simplifications are made and the problem is solved in the time domain using a Newmark time integration scheme. An overview of the formulation is provided below.

Hydroelastic Formulation

For hydroelastic analysis, it is convenient to define the vibratory blade motion as displacements ($\vec{\delta}$) superposed on the rigid blade motion:

$$\vec{\chi} = \vec{x} + \vec{\delta}(\vec{\chi}, t) \tag{15}$$

where $\vec{\chi}$ and $\vec{x}$ denote the position vectors to the deformed and undeformed blade surface, respectively.

Similar to the hydrodynamic formulation for rigid blades, the perturbation flow field is assumed to be incompressible, inviscid, and irrotational. Thus, the perturbation velocity can be represented as the gradient of the perturbation potential Φ, where $\nabla^2\Phi = 0$. Assuming linearity, Φ can be decomposed into two parts:

$$\Phi(\vec{\chi}, t) = \phi(\vec{x}, t) + \varphi(\vec{\chi}, t) \tag{16}$$

where $\phi(\vec{x}, t)$ denotes the potential due to rigid blades rotating in non-uniform wake, and $\varphi(\vec{\chi}, t)$ denotes the potential due to the vibrating blades in uniform wake.

Applying Taylor's expansion, the perturbation velocity can be approximated as follows,

$$\nabla\Phi = \nabla(\phi + \varphi) = \nabla\phi + \nabla\varphi + \vec{\delta} \cdot \nabla(\nabla\phi) \tag{17}$$

The gradient operator ∇ in Eqn. 17, and from here on, is evaluated on the undeformed blade surface $\vec{x}$. A detailed derivation of Eqn. 17 is given in Breslin's discussion of (Vorus 1981) and in (Kuo 1984). Assuming the contribution of the last term in Eqn 17 to be negligible compared to the first two terms, the perturbation velocity can be simplified as follows:

$$\nabla\Phi = \nabla\phi + \nabla\varphi \tag{18}$$

Accordingly, the total velocity $\vec{v}$ can be written as follows:

$$\vec{v}(\vec{\chi},t) = \vec{q}_{in}(\vec{x},t) + \nabla\Phi(\vec{\chi},t) = \vec{q}(\vec{x},t) + \nabla\varphi(\vec{\chi},t) \quad (19)$$

where $\vec{q}(\vec{x},t) = \vec{q}_{in}(\vec{x},t) + \nabla\phi(\vec{x},t)$ (i.e. Eqn. 2) is the fluid velocity due to rigid blades rotating in non-uniform wake; $\nabla\varphi(\vec{\chi},t)$ is the fluid velocity due to vibrating blades in uniform wake.

According to Bernoulli's equation, the total pressure (P_t) acting normal to the blade surface can be computed as follows:

$$\begin{aligned} \Delta P_t &= P_t - P_o \quad (20) \\ &= \rho\left[\frac{1}{2}|\vec{q}_w|^2 + \frac{1}{2}\omega^2 r^2 - gY - \frac{\partial\Phi}{\partial t} - \frac{1}{2}|\vec{v}|^2\right] \end{aligned}$$

where

$$\begin{aligned} \frac{\partial\Phi}{\partial t} &= \frac{\partial\phi}{\partial t} + \frac{\partial\varphi}{\partial t} \quad (21) \\ |\vec{v}|^2 &= |\vec{q}|^2 + 2\vec{q}\cdot\nabla\varphi + |\nabla\varphi|^2 \quad (22) \end{aligned}$$

The last term in Eqn. 22 can be dropped since the vibratory displacements are assumed to be small. Thus, ΔP_t can also be decomposed into two parts:

$$\Delta P_t = \Delta P + \Delta P_v \quad (23)$$

where

$$\Delta P = \rho\left[\frac{1}{2}|\vec{q}_w|^2 + \frac{1}{2}\omega^2 r^2 - gY - \frac{\partial\phi}{\partial t} - \frac{1}{2}|\vec{q}|^2\right] \quad (24)$$

$$\Delta P_v = \rho\left[-\frac{\partial\varphi}{\partial t} - \vec{q}\cdot\nabla\varphi\right] \quad (25)$$

ΔP is the pressure distribution if the blades were perfectly rigid; ΔP_v is the pressure distribution due to blade vibration.

Both ϕ and φ must satisfy the Laplace equation. Hence, Green's third identity is applied to determine the unknown potentials. For the rigid blade case, ϕ can be determined by applying the boundary conditions explained earlier in the "BEM Formulation" Section. For the vibrating blade case, φ is computed as follows:

$$\begin{aligned} 2\pi\varphi_p(t) = \int\int_{S_B(t)} \Bigg\{ & \varphi_q(t)\left[\frac{\partial G(p;q)}{\partial n_q(t)} - \frac{\partial G(p;\hat{q})}{\partial n_{\hat{q}}(t)}\right] \quad (26) \\ & - \left[G(p;q) - G(p;\hat{q})\right]\frac{\partial\varphi_q(t)}{\partial n_q(t)}\Bigg\} dS \\ + \int\int_{S_W(t)} \Bigg\{ & \Delta\varphi_q(t)\left[\frac{\partial G(p;q)}{\partial n_q(t)} - \frac{\partial G(p;\hat{q})}{\partial n_{\hat{q}}(t)}\right]\Bigg\} dS \end{aligned}$$

where φ_p is the induced potential at point p due to sources and dipoles representing the submerged part of the vibrating blade ($S_B(t)$) and wake ($S_W(t)$) surfaces. The negative image method is used to account for free surface effects. The subscripts q and $\hat{q}$ correspond to integration points on the real and image integration surfaces, respectively.

The wake dynamic boundary condition requires the pressure jump across the collapsed wake surface, $S_W(t)$, to be zero:

$$0 = P_v^+ - P_v^- = -\left[\frac{\partial}{\partial t}(\Delta\varphi) + \vec{q}\cdot\nabla(\Delta\varphi)\right] = -\frac{D}{Dt}(\Delta\varphi) \quad (27)$$

Thus, the dipole strength $\Delta\varphi(t)$ can be determined as follows:

$$\Delta\varphi(r,\theta,t) = \Delta\varphi\left(r_T, t - \frac{\theta-\theta_T}{\omega}\right) \quad (28)$$

where (r,θ) are the cylindrical coordinates at any point in the trailing wake surface, and (r_T,θ_T) are the blade trailing edge coordinates of the corresponding streamline.

The value of the dipole strength, $\Delta\varphi(r_T,t)$, at the trailing edge of the blade at radius r_T and time t, is given by Morino's Kutta condition (Morino & Kuo 1974):

$$\Delta\varphi(r_T,t) = \varphi^+(r_T,t) - \varphi^-(r_T,t) \quad (29)$$

where $\varphi^+(r_T,t)$ and $\varphi^-(r_T,t)$ are the values of the vibratory potential at the upper (suction side) and the lower (pressure side) blade trailing edge, respectively, at time t.

Defining $F(\vec{\chi},t)$ as the deformed blade surface rotating in non-uniform wake, the exact kinematic boundary conditions requires that

$$\frac{D}{Dt}F(\vec{\chi},t) = 0 \quad (30)$$

Via linear decomposition of the perturbation potential, it can be shown that Eqn. 30 reduces to the follow set of two equations (Kuo 1984):

$$\frac{\partial\phi}{\partial n} = -\vec{q}_{in}\cdot\vec{n} \quad (31)$$

$$\frac{\partial\varphi}{\partial n} = \frac{\partial\vec{\delta}}{\partial t}\cdot\vec{n} + \left[(\nabla\phi\cdot\nabla)\vec{\delta} - (\vec{\delta}\cdot\nabla)(\nabla\phi)\right]\cdot\vec{n} \quad (32)$$

where Eqn. 31 is the kinematic boundary condition for the rigid blade case (same as Eqn. 6), and Eqn. 32 is the kinematic boundary condition for the elastic blade case. A detailed derivation of the above equations can be found in Breslin's discussion of (Vorus 1981) and in (Kuo 1984). Assuming the contribution of the terms inside the square bracket to be negligible, Eqn. 32 can be simplified as follows:

$$\frac{\partial\varphi}{\partial n} = \frac{\partial\vec{\delta}}{\partial t}\cdot\vec{n} \quad (33)$$

By considering the above boundary conditions, Eqn. 26 can be rewritten in matrix form as follows:

$$[A_v]\{\varphi\} = [B_v]\left\{\frac{\partial \varphi}{\partial n}\right\} \tag{34}$$

where $[A_v]$ and $[B_v]$ are the dipole and source influence coefficient matrices, respectively. Multiplying both sides of Eqn. 34 by $[A_v]^{-1}$ yields the solution for $\{\varphi\}$:

$$\{\varphi\} = [A_v]^{-1}[B_v]\left\{\frac{\partial \varphi}{\partial n}\right\} = [C_v]\left\{\frac{\partial \varphi}{\partial n}\right\} \tag{35}$$

where $[C_v] = [A_v]^{-1}[B_v]$.

To determine the blade displacement vectors, the equilibrium equation of motion is solved via finite element method:

$$[M]\{\ddot{u}\} + [B]\{\dot{u}\} + [K]\{u\} = \{\mathcal{F}\} \tag{36}$$

where [M], [B], and [K] are the standard structural mass, damping, and stiffness matrices, respectively. $\{\ddot{u}\}$, $\{\dot{u}\}$, and $\{u\}$ are the nodal acceleration, velocity, and displacement vectors, respectively. The derivation of Eqn. 36 are given in standard FEM texts such as (Zienkiewicz 2000).

The nodal force vector, $\{\mathcal{F}\}$, can be decomposed into two parts:

$$\{\mathcal{F}\} = \{F\} + \{f\} \tag{37}$$

where $\{F\}$ is the nodal force vector due to rigid blades rotating in non-uniform inflow, and $\{f\}$ is the nodal force vector due to blade vibration:

$$\{F\} = -\int [N]^T \{\Delta P\} dS \tag{38}$$

$$\{f\} = -\int [N]^T \{\Delta P_v\} dS \tag{39}$$

where $[N]$ is the shape function for transforming the surface tractions (pressure acting normal to the elements) to consistent nodal forces.

Since $\{\Delta P\}$ is the pressure vector due to the non-vibrating blades, it can be computed separately via Eqn. 24 using the procedure explained in the "HYDRODYNAMIC FORMULATION" Section. On the other hand, $\{\Delta P_v\}$ is the pressure vector due to blade vibration, which depends on the unknown structural displacements.

Defining $[T]$ as the transformation matrix which relates the normal velocities at element centroids to the elemental nodal velocities:

$$\{\frac{\partial \vec{\delta}}{\partial t} \cdot \vec{n}\} = [T]\{\dot{u}\} \tag{40}$$

The following expression for φ can be obtained by combining Eqns. 33, 35, and 40:

$$\{\varphi\} = [C_v][T]\{\dot{u}\} \tag{41}$$

Recognizing that $[C_v]$ and $[T]$ are not functions of time, the partial time derivative of φ can be computed as follows:

$$\left\{\frac{\partial \varphi}{\partial t}\right\} = [C_v][T]\{\ddot{u}\} \tag{42}$$

Thus, the pressure vector due to blade vibration (Eqn. 25) can be rewritten as follows:

$$\{\Delta P_v\} = -\rho[C_v][T]\{\ddot{u}\} - \rho[QD][C_v][T]\{\dot{u}\} \tag{43}$$

where $[QD]$ is the matrix operator representing $\vec{q} \cdot \nabla$.

In the FEM model, the Newmark update formulas (Newmark 1959) are used for the time integration:

$$\begin{aligned} \{\dot{u}\}_{n+1} &= \{\dot{u}\}_n \\ &+ \Delta t\left[(1-\gamma)\{\ddot{u}\}_n + \gamma\{\ddot{u}\}_{n+1}\right] \end{aligned} \tag{44}$$

$$\begin{aligned} \{u\}_{n+1} &= \{u\}_n + \Delta t\{\dot{u}\}_n \\ &+ \frac{\Delta t^2}{2}\left[(1-2\alpha)\{\ddot{u}\}_n + 2\alpha\{\ddot{u}\}_{n+1}\right] \end{aligned} \tag{45}$$

where $\Delta t = t_{n+1} - t_n$ and the subscript n is used to index the time steps. To ensure stability and second order accuracy, $\gamma = 1/2$ and $\alpha = 1/4$ are used.

The solution to the equilibrium equation of motion (Eqn. 36) is obtained via an iterative strategy, which is implemented by means of a predictor-multicorrector scheme. At each time step, a series of corrected solutions are computed starting from an initial or predicted value. The iterations continue until a specified convergence has obtained. The highest time derivative is chosen as the vector of primary unknowns, namely $\{\ddot{u}\}_{n+1}$. Using a truncated Taylor's series expansion, Eqn. 36 can be written as follows:

$$\left([M] + \gamma\Delta t[B] + \alpha\Delta t^2[K]\right)\{\Delta\ddot{u}\}^{(i)}_{n+1} = \{\mathcal{R}\}^{(i)}_{n+1} \tag{46}$$

where the superscript i is used to index the non-linear iterations within each time step. The residual, $\{\mathcal{R}\}$, is calculated as follows:

$$\begin{aligned} \{\mathcal{R}\}^{(i)}_{n+1} &= \{F\}_{n+1} + \{f\}^{(i)}_{n+1} \\ &- \left([M]\{\ddot{u}\}^{(i)}_{n+1} + [B]\{\dot{u}\}^{(i)}_{n+1} + [K]\{u\}^{(i)}_{n+1}\right) \end{aligned} \tag{47}$$

where

$$\{f\}^{(i)}_{n+1} = -[M_a]\{\ddot{u}\}^{(i)}_{n+1} - [B_a]\{\dot{u}\}^{(i)}_{n+1} \tag{48}$$

$[M_a]$ and $[B_a]$ are the hydrodynamic added mass and damping matrices, respectively, due to blade vibration:

$$\begin{aligned} [M_a] &= \rho\int [N]^T[C_v][T]dS \\ [B_a] &= \rho\int [N]^T[QD][C_v][T]dS \end{aligned} \tag{49}$$

Iterations are not needed for $\{F\}$ since it does not depend on the vibratory blade motion. At each subsequent iteration, the correctors are computed as follows:

$$\{\ddot{u}\}_{n+1}^{(i+1)} = \{\ddot{u}\}_{n+1}^{(i)} + \{\Delta\ddot{u}\}_{n+1}^{(i)} \quad (50)$$

$$\{\dot{u}\}_{n+1}^{(i+1)} = \{\dot{u}\}_{n+1}^{(i)} + (\gamma\Delta t)\{\Delta\ddot{u}\}_{n+1}^{(i)} \quad (51)$$

$$\{u\}_{n+1}^{(i+1)} = \{u\}_{n+1}^{(i)} + (\alpha\Delta t^2)\{\Delta\ddot{u}\}_{n+1}^{(i)} \quad (52)$$

The above correctors ensure that every set of iterated values $\left(\{\ddot{u}\}_{n+1}^{(i+1)}, \{\dot{u}\}_{n+1}^{(i+1)}, \{u\}_{n+1}^{(i+1)}\right)$ adheres to the Newmark update formulas. The time integration and iterative strategies explained above follows the work of (Prevost 1997), which has shown to be unconditionally stable for coupled field problems.

The natural frequencies and mode shapes of the blades can be computed as follows:

$$([M] + [M_a])\{\ddot{\Psi}\} + ([B] + [B_a])\{\dot{\Psi}\} + [K]\{\Psi\} = 0 \quad (53)$$

where $\{\Psi\}$ is the vector of mode shapes. Equation 53 needs to be solved for each blade angle because both $[M_a]$ and $[B_a]$ change with blade submergence for surface-piercing propellers.

Preliminary Results

The implementation of the hydroelastic coupling is still underway. The structural part is modeled using a 3-D FEM code, DYNAFLOW, developed by Professor Prevost of Princeton University (Prevost 2000) over the last 20 years. Preliminary results for propellers 4381 (0^o skew) and 4383 (72^o skew) in air are shown in Figs. 22 and 23, respectively. Both propellers are 5-bladed, and the geometries are given in (Boswell 1971, Cumming et al 1972). These propellers were selected because systematic experimental measurements (Boswell 1971, Cumming et al 1972, Boswell et al 1976) and numerical predictions (Kuo 1984, Kuo & Vorus 1985) of the blade loads and static stress distributions are available in open literature. Preliminary comparisons of the predicted natural frequencies and mode shapes with those presented in (Kuo 1984, Kuo & Vorus 1985) seem encouraging. However, additional work is needed to fully implement the coupling algorithm for surface-piercing propellers.

CONCLUSIONS

A 3-D BEM, PROPCAV, has been extended for the analysis of partially submerged propellers. An overview of the formulation and solution method was described. Comparisons with experimental measurements for propeller model 841-B were presented. In general, the predicted ventilated cavity planforms and propeller loadings compared well with experimental measurements and observations. The method also appeared to converge quickly with number of panels. However, there were some discrepancies between the predicted and measured dynamic blade performance, particularly at high rotational speeds. The discrepancies can be attributed to the inability of the present BEM to model the effects of blade vibration, jet sprays, and rise in overall free surface elevation. To account for the effects of blade vibration, the authors are in the process of coupling the BEM with a FEM to model fluid-structure interactions. An overview of the coupling algorithm and preliminary results were presented. The authors are also in the process of developing a fully non-linear 2-D BEM to study the effect of jet sprays generated at the moment of impact for a surface-piercing hydrofoil. Preliminary results were presented in (Young & Kinnas 2002). The ultimate goal of this research is to develop a robust and reliable tool to predict the hydro- and elasto-dynamic performance of surface-piercing propellers.

ACKNOWLEDGMENT

Support for this research was provided by Phase III of the "Consortium on Cavitation Performance of High Speed Propulsors" with the following members: AB Volvo Penta, American Bureau of Shipping, El Pardo Model Basin, Hyundai Maritime Research Institute, Kamewa AB, Michigan Wheel Corporation, Naval Surface Warfare Center Carderock Division, Office of Naval Research (Contract N000140110225), Ulstein Propeller AS, VA Tech Escher Wyss GMBH, and Wärtsilä Propulsion.

REFERENCES

Alder, R. and Moore, D. 1977 Performance of an inclined shaft partially-submerged propeller operating over a range of shaft yaw angles. Technical report. SPD-802-01. Naval Ship Resesarch and Development Center.

Allison, J. 1978 Propellers for high-performance craft. *Marine Technology*, **15**, 4, October, pp. 335–380.

Atkinson, P. 1968 On the choice of method for the calculation of stress in marine propellers. *Transactions, Royal Institution of Naval Architecture*, **110**.

Atkinson, P. 1973 The prediction of marine propeller distortion and stresses using a superparametric thick shell finite-elelement model. *Transactions, Royal Institution of Naval Architecture*, **115**.

Boswell, R. 1971 Design, cavitation performance and open-water performance of a series of research skewed propellers. Technical report. 3339. DTNSRDC.

Boswell, R., Miller, M. and Kader, R. 1976 Static stress measurements on a series of skewed propeller blades with and without forward rake. Technical report. Report SPD-712-01. David Taylor Model Basin. Aug.

Brandt, H. 1973 Modellversuche mit schiffspropellern an der wasseroberfläche. *Schiff und Hafen*, **25**, 5, pp. 415–422.

Brillouin, M. 1911 Les surfaces de glissement de Helmholtz et la resistance des fluides. *Annales de Chimie and de Physique*, **vol. 23**, pp. 145–230.

Brooks, J. 1980 Vibrations of a marine propeller operating in a nonuniform inflow. Technical report. Report DTNSRDC-80/056. David Taylor Research Center. April.

Choi, J. 2000 Vortical inflow – propeller interaction using unsteady three-dimensional euler solver. Doctoral dissertation, Department of Civil Engineering, The University of Texas at Austin. August.

Cumming, R. A., Morgan, W. B. and Boswell, R. J. 1972 Highly skewed propellers. In: *Transactions*. Society of Naval Architects and Marine Engineers.

Dashnaw, F. and Reed, F. 1971 Propeller strain measurements on the s.s. michigan. *Marine Technology*, **8**, 4, pp. 486–509.

Dobay, G. 1970 Unsteady blade force measurements on a skewed partially-submerged propeller. Technical report. 392-H-01. Naval Ship Resesarch and Development Center. June.

Dyson, P. K. 2000 The modelling, testing and design, of a surface piercing propeller drive. Doctoral dissertation, Department of Mechanical and Marine Engineering, Plymouth University. October.

Dyson, P. K., Chudley, J. and Grieve, D. 2000 An experimental programme to determine the mean and time varying loads imposed by surface piercing propellers. Sea Australia 2000, Sydney.

Ferrando, M. and Scamardella, A. 1996 Surface piercing propellers: Testing methodologies, results analysis and comments on the open water characteristics. *Proceedings:* Small Craft Symposium.

Fine, N. E. 1992 Nonlinear analysis of cavitating propellers in nonuniform flow. Doctoral dissertation, Department of Ocean Engineering, Massachusetts Institute of Technology. October.

Fine, N. and Kinnas, S. 1993a A boundary element method for the analysis of the flow around 3-d cavitating hydrofoils. *Journal of Ship Research*, **37**, September, 213–224.

Fine, N. and Kinnas, S. 1993b The nonlinear numerical prediction of unsteady sheet cavitation for propellers of extreme geometry. *Proceedings:* Sixth International Conference On Numerical Ship Hydrodynamics. August, 531–544.

Furuya, O. 1984 A performance prediction theory for partially submerged ventilated propellers. *Proceedings:* Fifteenth Symposium on Naval Hydrodynamics.

Furuya, O. 1985 A performance prediction theory for partially submerged ventilated propellers. *Journal of Fluid Mechanics*, **151**, pp. 311–335.

Genalis, P. 1970 Elastic strength of propellers - an anlysis by matrix methods. Technical report. Report 3397. David Taylor Research Center.

Greeley, D. and Kerwin, J. 1982 Numerical methods for propeller design and analysis in steady flow. *Trans. SNAME*, **vol 90**.

Hadler, J. and Hecker, R. 1968 Performance of partially submerged propellers. *Proceedings:* The 7th ONR Symposium on Naval Hydrodynamics. August.

Hecker, R. 1973 Experimental performance of a partially submerged propeller in inclined flow. SNAME Spring Meeting, Lake Buena Vista, FL, April.

Hecker, R. and Crown, D. 1970 Performance characteristics of partially-submerged propeller 4281 with varying number of blades at low advance coefficients. Technical report. 249-H-12. Naval Ship Resesarch and Development Center. November.

Helle, H. and Hageman, L. 1980 Fatigue damage accumulation in marine propellers. *International Shipbuilding Progress*, **27**, 312, pp. 193–210.

Hsin, C.-Y. 1990 Development and analysis of panel method for propellers in unsteady flow. Doctoral dissertation, Department of Ocean Engineering, Massachusetts Institute of Technology. September.

Kerwin, J., Kinnas, S., Lee, J.-T. and Shih, W.-Z. 1987 A surface panel method for the hydrodynamic analysis of ducted propellers. *Trans. SNAME*, **95**.

Kinnas, S. and Fine, N. 1991 Non-Linear Analysis of the Flow Around Partially or Super-Cavitating Hydrofoils by a Potential Based Panel Method. *Proceedings:* Boundary Integral Methods-Theory and Applications, Proceedings of the IABEM-

90 Symposium, Rome, Italy, October 15-19, 1990. Springer-Verlag, Heidelberg, 289–300.

Kinnas, S. and Fine, N. 1992 A nonlinear boundary element method for the analysis of unsteady propeller sheet cavitation. *Proceedings:* Nineteenth Symposium on Naval Hydrodynamics. August, 717–737.

Kinnas, S. and Fine, N. 1993 A numerical nonlinear analysis of the flow around two- and three-dimensional partially cavitating hydrofoils. *Journal of Fluid Mechanics*, **254**, September, 151–181.

Kinnas, S. and Hsin, C.-Y. 1992 A boundary element method for the analysis of the unsteady flow around extreme propeller geometries. *AIAA Journal*, **30**, 3, March, 688–696.

Kinnas, S., Choi, J., Lee, H. and Young, J. 2000 Numerical cavitation tunnel. *Proceedings:* NCT50, International Conference on Propeller Cavitation. April 3-5.

Kruppa, C. F. L. 1972 Testing partially submerged propellers. *Proceedings:* 13th ITTC Report of Cavitation Committee. Appendix V.

Kruppa, C. F. L. 1992 Testing surface piercing propellers. *Proceedings:* Hydrodynamics : Computations, Model Tests, and Reality. May, pp. 107–113.

Kudo, T. and Kinnas, S. 1995 Application of vortex/source lattice method on supercavitating propellers. *Proceedings:* 24th American Towing Tank Conference. November 2-3.

Kudo, T. and Ukon, Y. 1994 Calculation of supercavitating propeller performance using a vortex-lattice method. *Proceedings:* Second International Symposium on Cavitation. April 5-7, 403–408.

Kuo, J. 1984 Analysis of propeller blade dynamic stresses. Doctoral dissertation, Department of Naval Architecture and Marine Engineering, The University of Michigan, Ann Arbor, MI.

Kuo, J. and Vorus, W. 1985 Propeller blade dynamic stress. *Proceedings:* Tenth Ship Technology and Research (STAR) Symposium. May 21-24, pp. 39–69.

Lee, H. S. 2002 Modeling of developed tip vortex cavitation and unsteady wake alignment. Doctoral dissertation, Department of Civil Engineering, The University of Texas at Austin. August.

Lee, H. and Kinnas, S. 2002 Fully unsteady wake alignment for propellers in non-axisymmetric flows. *Proceedings:* Journal of Ship Research. Submitted for publication.

Lee, J.-T. 1987 A potential based panel method for the analysis of marine propellers in steady flow. Doctoral dissertation, Department of Ocean Engineering, Massachusetts Institute of Technology. August.

Lewis, E. 1989 Vibration. *Principles of Naval Architecture*, **2**, Chapter 7.

Miller, W. and Szantyr, J. 1998 Model experiments with surface piercing propellers. *Ship Technology Research*, **45**, February, pp. 14–21.

Morgan, W. 1954 An approximate method of obtaining stress in a propeller blade. Technical report. Report 919. David Taylor Research Center.

Morino, L. and Kuo, C.-C. 1974 Subsonic Potential Aerodynamic for Complex Configurations : A General Theory. *AIAA Journal*, **vol 12**, no 2, February, pp 191–197.

Mueller, A. and Kinnas, S. 1999 Propeller sheet cavitation predictions using a panel method. *Journal of Fluids Engineering*, **121**, June, 282–288.

Newmark, N. 1959 A method of computation for structural dynamics. *Journal of Engineering Mechanics*, pp. 67–94.

Nozawa, K. and Takayama, N. 2002a Experimental study on propulsive performance of surface piercing propeller. *Journal of the Kansai Society of Naval Architects.*

Nozawa, K. and Takayama, N. 2002b Hydrodynamic performance and exciting force of surface piercing propeller. *Proceedings:* Asia Pacific Workshop on Marine Hydrodynamics (APHydro 2002). May 21-23.

Oberembt, H. 1968 Zur bestimmung der instationären flügelkräfte bei einem propeller mit aus dem wasser herausschlagenden flügeln. Technical report. Inst. für Schiffau der Universität Hamburg, Bericht Nr. 247. Juli.

Olofsson, N. 1996 Force and flow characteristics of a partially submerged propeller. Doctoral dissertation, Department of Naval Architecture and Ocean Engineering, Chalmers University of Technology, Göteborg, Sweden. February.

Olofsson, N. 2001 Letter to the author and professor. s. a. kinnas. January 20.

Prevost, J. 1997 Partitioned solution proceedure for simultaneous integration of coupled-field problems. *Comm. in Num. Meth. in Eng.*, **13**, pp. 239–247.

Prevost, J. 2000 Dynaflow: A nonlinear transient finite element analysis program. Technical report. Princeton University.

RAINS, D. A. 1981 Semi-submerged propellers for monohull displacement ships. *Proceedings:* Propeller '81 Symposium. Society of Naval Architects and Marine Engineers, Virginia Beach, VA, May 26-27, pp. 15–40.

REYNOLDS, O. 1874 On the effect of immersion on screw propellers. *Transactions of Institute of Naval Architecture*, **2**.

ROSE, J. C. AND KRUPPA, C. F. L. 1991 Surface piercing propellers - methodical series model test results. *Proceedings:* FAST'91. June.

ROSE, J. C., KRUPPA, C. F. L. AND KOUSHAN, K. 1993 Surface piercing propellers - propeller/hull interaction. *Proceedings:* FAST'93. December, pp. 867–881.

SAVINEAU, C. AND KINNAS, S. 1995 A numerical formulation applicable to surface piercing hydrofoils and propellers. *Proceedings:* 24th American Towing Tank Conference.

SCHOENHERR, K. 1963 Formulation of propeller blade strength. *Proceedings:* Spring Meeting, The Society of Naval Architects and Marine Engineers. April 25-27.

SHIBA, H. 1953 Air-drawing of marine propellers. Technical report. 9. Transportation Technical Research Institute. August.

SHIELDS, C. 1968 Performance characteristics of several partially submerged supercavitating propellers. Technical report. 2723. Naval Ship Resesarch and Development Center. July.

TABBARA, M., BLACKER, T. AND BELYTSCHKO, T. 1994 Finite element derivative recovery by moving least squares interpolants. *Computational Methods in Applied Mechanical Engineering*, **117**, pp. 211–223.

TAYLOR, D. 1933 The speed and power of ships. Technical report. U.S. Governmnet Printing Office, Wahsington, D.C.

TSUSHIMA, H. 1972 Dynamic response of an elastic propeller to a non-uniform inflow. Doctoral dissertation, Department of Aerospace Engineering, Pennsylvania State University.

VILLAT, H. 1914 Sur la validité des solutions de certain problem d' hydrodynamique. *Journal de Mathematiques*, **vol 6**, No. 10, pp 231–290.

VORUS, W. S. 1991 Forces on surface-piercing propellers with inclination. *Journal of Ship Research*, **35**, 3, pp. 210–218.

VORUS, W. 1981 Hydrodynamic added-mass matrix of vibrating ship based on a distribution of hull surface sources. *SNAME Transactions*, **89**, pp. 397–416.

WANG, D. 1977 Water entry and exit of a fully ventilated foil. *Journal of Ship Research*, **21**, pp. 44–68.

WANG, D. 1979 Oblique water entry and exit of a fully ventilated foil. *Journal of Ship Research*, **23**, pp. 43–54.

WANG, G., ZHU, X. AND SHENG, Z. 1990a Hydrodynamic forces of a three-dimensional fully ventilated foil entering water. *Journal of Hydrodynamics*, **5**, 2.

WANG, G., JIA, D. AND SHENG, Z. 1990b Hydrodynamic performance of partially submerged ventilated propeller. *Shipbuilding of China*.

WANG, G., JIA, D. AND SHENG, Z. 1992 Study on propeller characteristics near water surface. *Proceedings:* The 2nd Symposium on Propeller and Cavitation. September 1-4, pp. 161–168.

WANG, S. Y. 1995 Systemtische analyse von modellversuchen mit teilgetauchten propellrn. Doctoral dissertation, Technischen Unversitaet Berlin (D83).

YEGOROV, I. AND SADOVNIKOV, Y. 1961 Effect of instability on hydrodynamic characteristics of a propeller cutting the water surface. *Sudostroyenige*, pp. 15–17.

YOUNG, Y. L. 2002 Numerical modeling of supercavitating and surface-piercing propellers. Doctoral dissertation, Department of Civil Engineering, The University of Texas at Austin. May.

YOUNG, Y. AND KINNAS, S. 2000 Prediction of unsteady performance of surface-piercing propellers. *Proceedings:* 2000 Propeller and Shaft Symposium. Society of Naval Architects and Marine Engineers, Virginia Beach, VA, September 20-21.

YOUNG, Y. AND KINNAS, S. 2001 A BEM for the prediction of unsteady midchord face and/or back propeller cavitation. *Journal of Fluids Engineering*, **123**, June, pp. 311–319.

YOUNG, Y. AND KINNAS, S. 2002 A BEM technique for the modeling of supercavitating and surface-piercing propeller flows. 24^{th} *Symposium on Naval Hydrodynamics*, July 8-13.

YOUNG, Y. AND KINNAS, S. 2003a Analysis of supercavitating and surface-piercing propeller flows via bem. *Accepted to the Special Issue of Computational Mechanics Journal*.

YOUNG, Y. AND KINNAS, S. 2003b Numerical modeling of supercavitating propeller flows. *Journal of Ship Research*, **47**, 1, March, pp. 48–62.

YOUNG, Y. AND KINNAS, S. 2003c Performance prediction of surface-piercing propellers. *Submitted to Journal of Ship Research.*

ZIENKIEWICZ, O. 2000 *The Finite Element Method, 5th Edition.* Oxford.

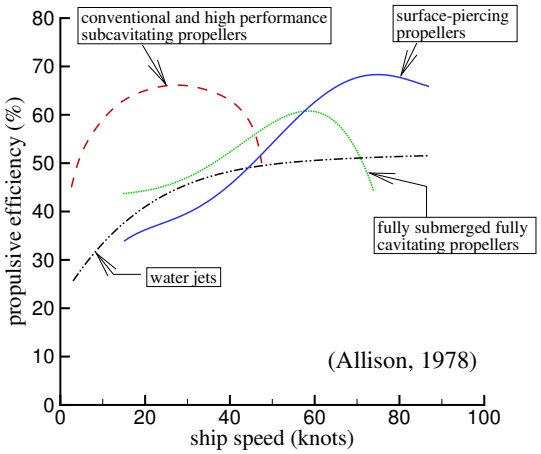

Figure 1: Approximate maximum installed efficiency envelopes for different propellers. Taken from (Allison, 1978).

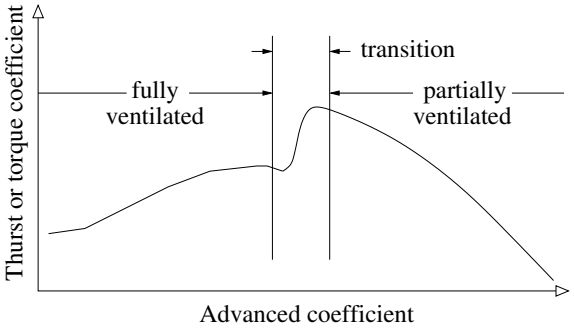

Figure 2: Schematic diagram of the three major flow regimes. Shown in (Young & Kinnas 2003c).

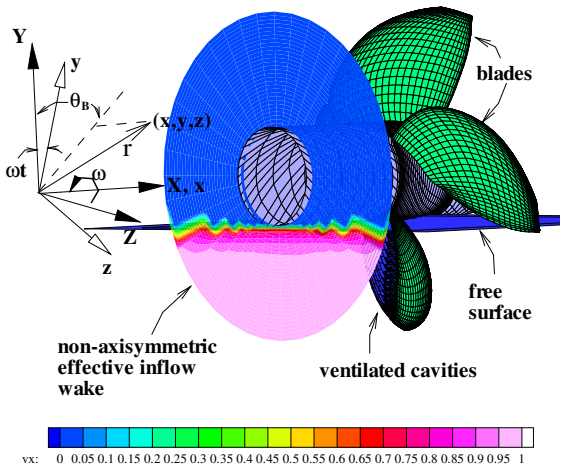

Figure 3: A partially ventilated surface-piercing propeller subjected to a general inflow wake. The blade-fixed (x, y, z) and ship-fixed (X, Y, Z) coordinate systems are shown. Shown in (Young & Kinnas 2003c).

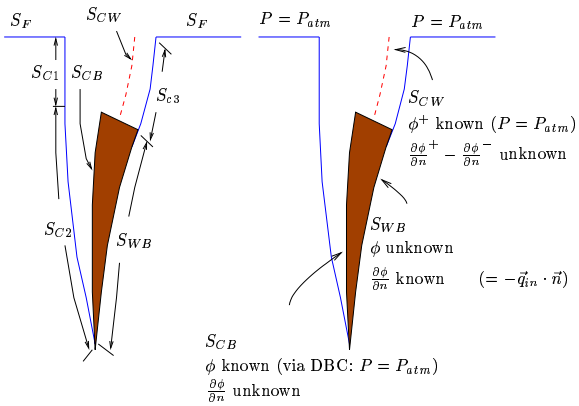

Figure 4: Definition of "exact" and approximated flow boundaries around a surface-piercing blade section. Shown in (Young & Kinnas 2003c).

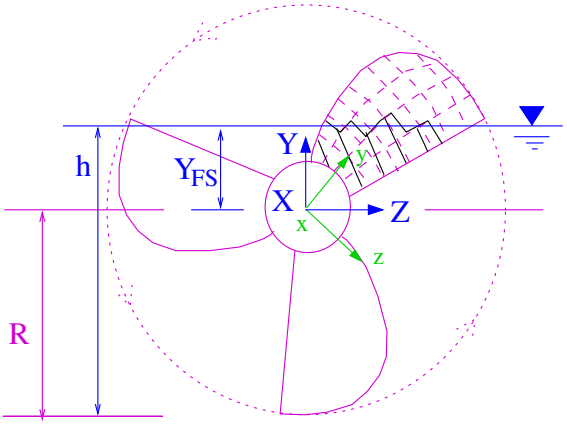

Figure 5: Definition of ship-fixed (X, Y, Z) and blade-fixed (x, y, z) coordinate systems.

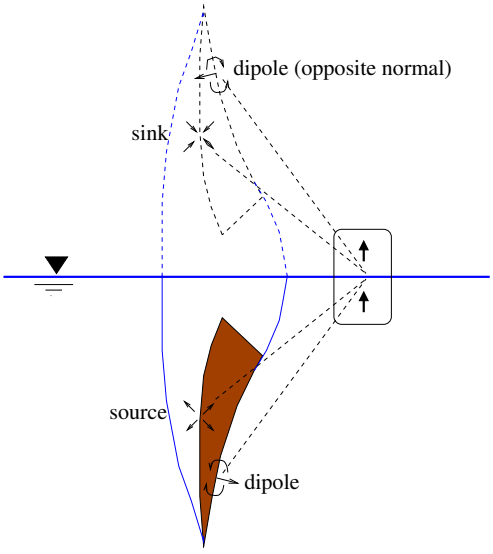

Figure 6: Schematic example of the negative image method on a partially submerged blade section. Shown in (Young & Kinnas 2003c).

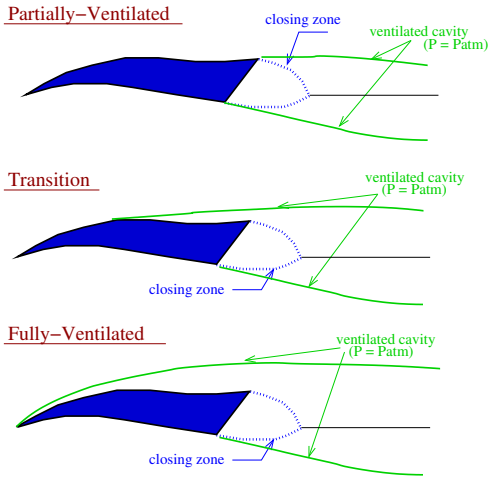

Figure 7: Treatment for surface-piercing blade sections with non-zero thickness blade trailing edge. Shown in (Young & Kinnas 2003c).

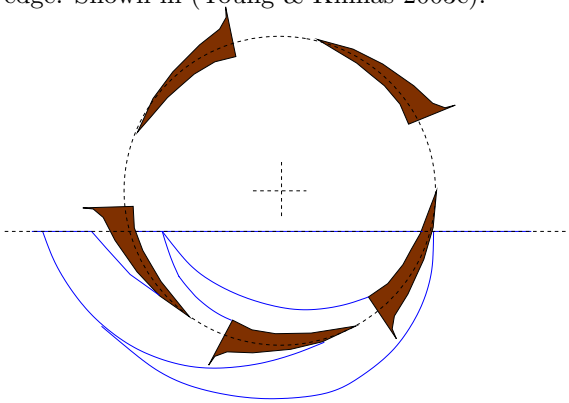

Figure 8: Graphic illustration of ventilated cavity patterns that satisfy the cavity detachment condition on a partially submerged blade section. Shown in (Young & Kinnas 2003c).

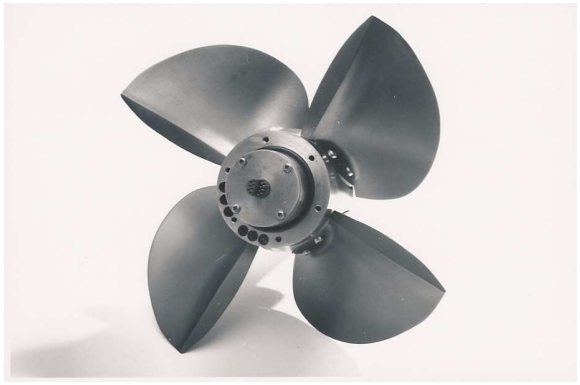

Figure 9: Photograph of propeller model 841-B. Taken from (Olofsson 1996).

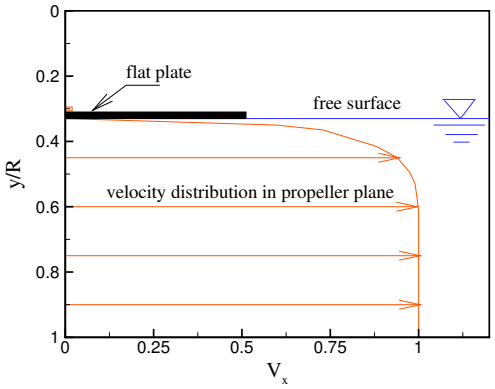

Figure 10: Axial velocity distribution at the propeller plane. Based on data from (Olofsson 1996).

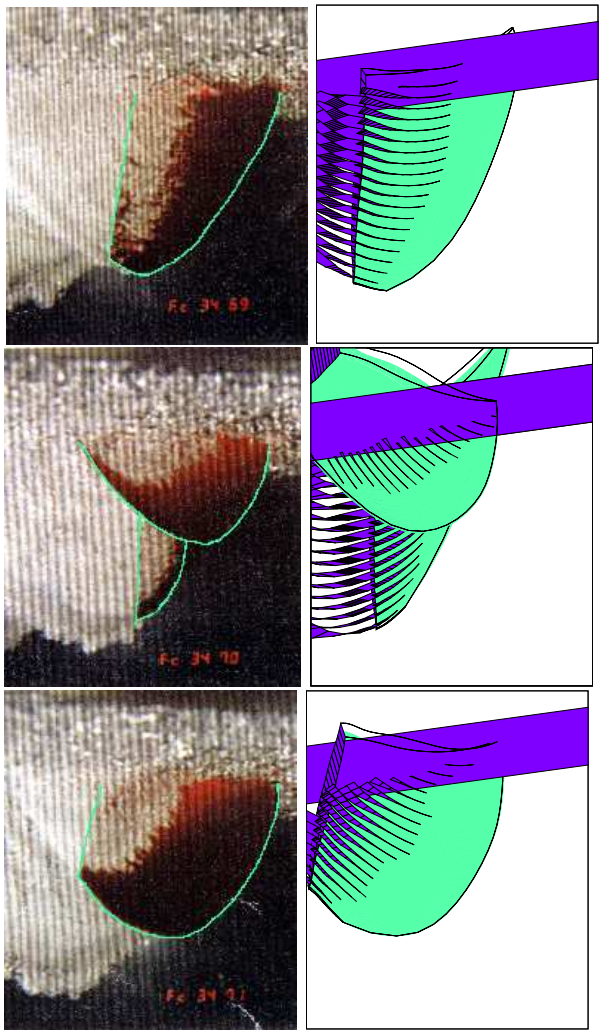

Figure 11: Comparison of the observed(left) and predicted(right) ventilation patterns. Propeller M841B. $J_A = 1.2$. $\lambda = 9$. $F_r = 6$. Shown in (Young & Kinnas 2003c).

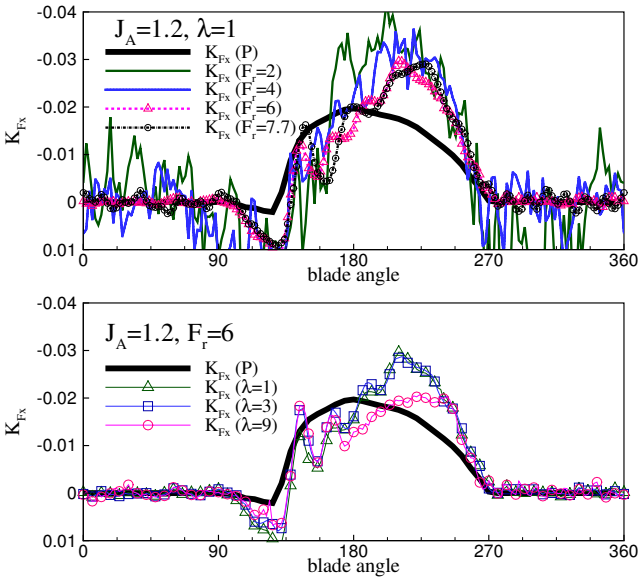

Figure 12: Effect of Froude number (top) and cavitation number (bottom) on the axial force coefficients in the blade-fixed coordinates for $J_A = 1.2$.

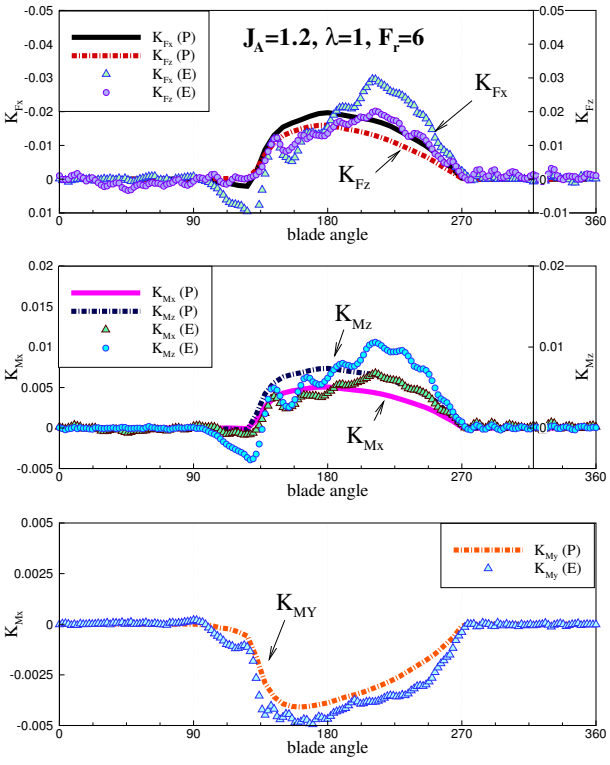

Figure 13: Comparison of predicted (P) and measured (E) blade forces for $J_A = 1.2$.

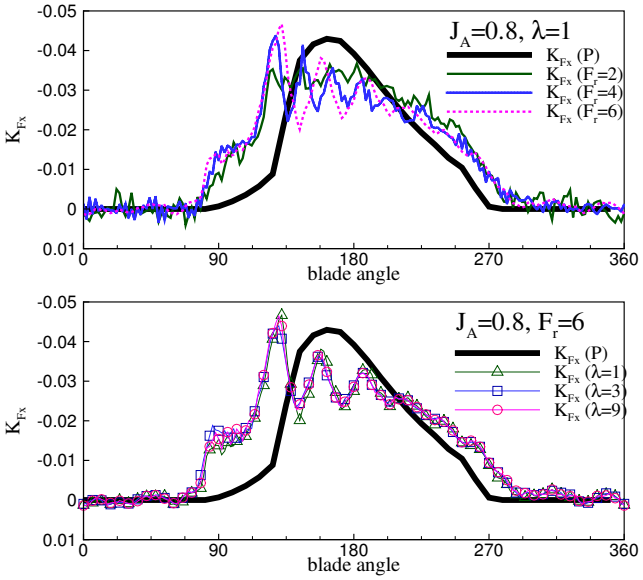

Figure 14: Effect of Froude number (top) and cavitation number (bottom) on the axial force coefficients in the blade-fixed coordinates for $J_A = 0.8$.

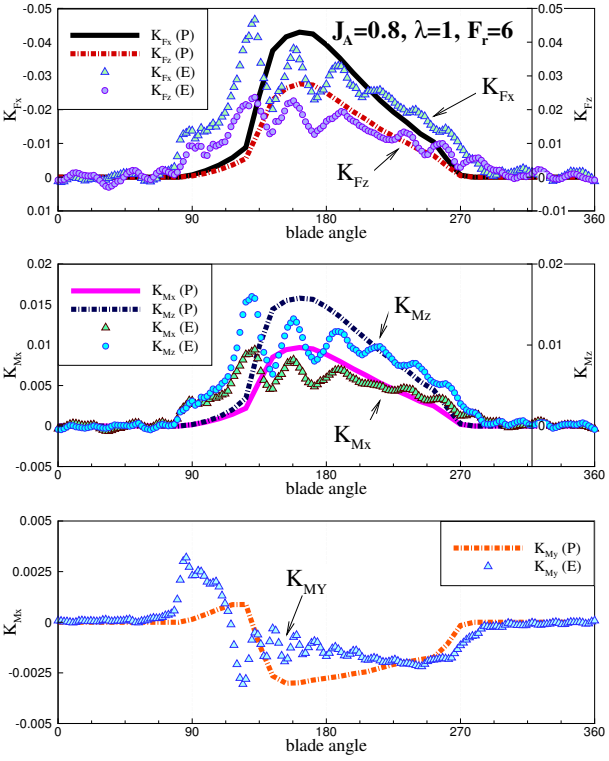

Figure 15: Comparison of predicted (P) and measured (E) blade forces for $J_A = 0.8$.

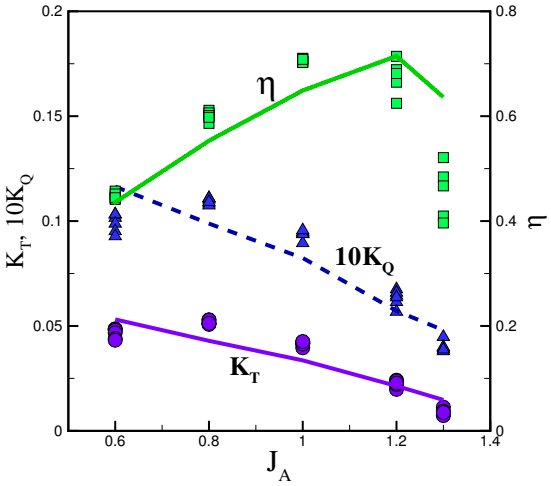

Figure 16: Averaged performance characteristics of propeller model 841-B in ship-fixed coordinates. The lines and symbols represent the numerical predictions and experimental measurements, respectively. Shown in (Young & Kinnas 2003c).

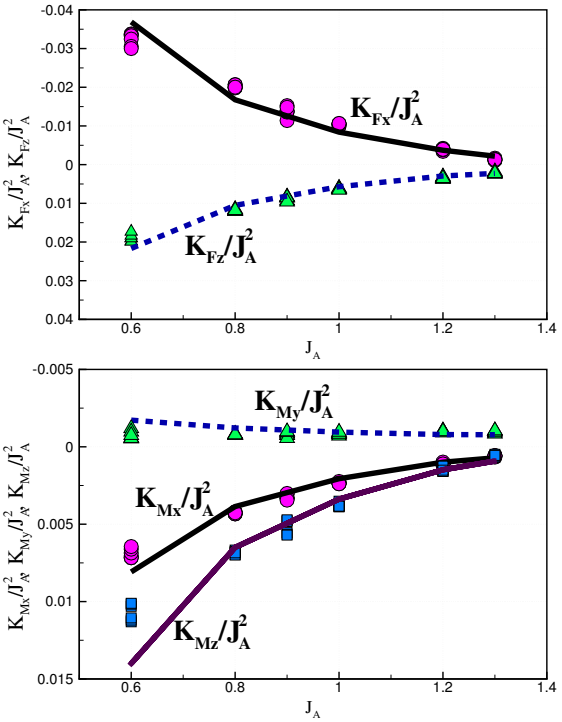

Figure 17: Averaged individual force and moment coefficients of propeller model 841-B in blade-fixed coordinates. The lines and symbols represent the numerical predictions and experimental measurements, respectively. Shown in (Young & Kinnas 2003c).

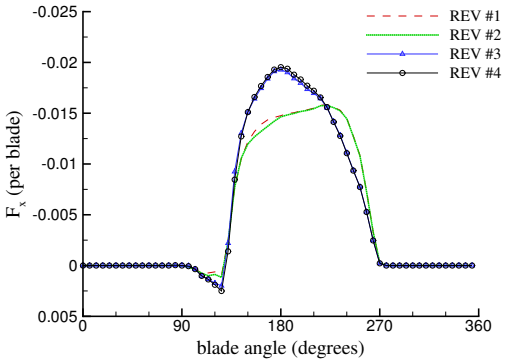

Figure 18: Convergence of thrust (K_T) and torque (K_Q) coefficients (per blade) with number of revolutions. Propeller model 841-B. $J_A = 1.2$. 70x30 panels. $\Delta\theta = 6^o$.

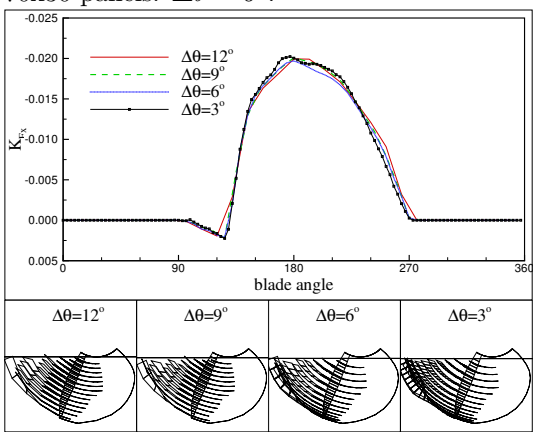

Figure 19: Convergence of thrust (K_T) and torque (K_Q) coefficients (per blade) with time step size. Propeller model 841-B. $J_A = 1.2$. 70x30 panels. 6 propeller revolutions. Shown in (Young & Kinnas 2003c).

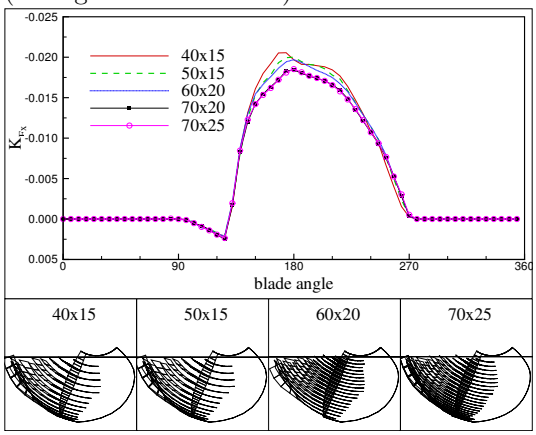

Figure 20: Convergence of thrust (K_T) and torque (K_Q) coefficients (per blade) with panel discretization. Propeller model 841-B. $J_A = 1.2$. $\Delta\theta = 6^o$. 6 propeller revolutions. Shown in (Young & Kinnas 2003c).

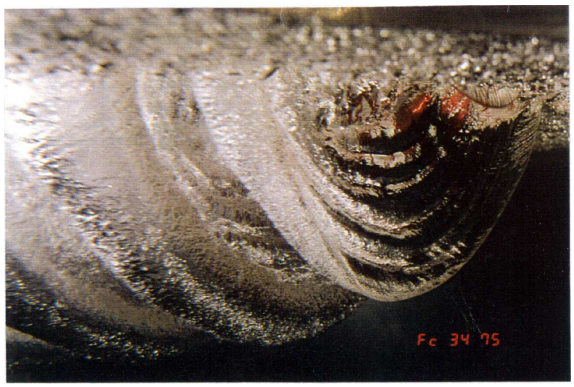

Figure 21: Ringing patterned observed on the ventilated cavities due to resonant blade vibration. $\lambda = 1$. $J_A = 0.8$. $F_r = 6.0$. Taken from (Olofsson 1996).

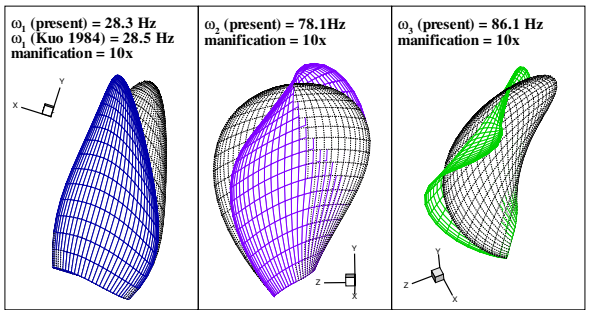

Figure 22: Predicted natural frequencies and mode shapes of propeller 4381 (0^o skew) in air.

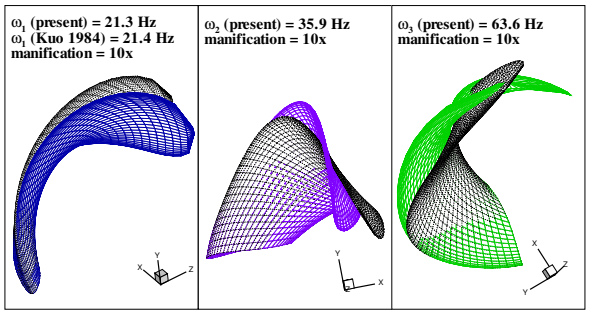

Figure 23: Predicted natural frequencies and mode shapes of propeller 4383 (72^o skew)in air.